Volume 9 | Number 17 | 7 September 2025

MATERIALS CHEMISTRY

FRONTIERS

CCS 中国化学会 CHINESE CHEMICAL SOCIETY
ICCAS 1956
ROYAL SOCIETY OF CHEMISTRY
rsc.li/frontiers-materials

MATERIALS CHEMISTRY FRONTIERS

CHINESE CHEMICAL SOCIETY

ROYAL SOCIETY OF CHEMISTRY

RESEARCH ARTICLE

View Article Online
View Journal | View Issue

Cite this: *Mater. Chem. Front.*, 2025, **9**, 2590

Rational design of lead-free $CsCu_2I_3$@g-C_3N_4 composite for efficient energy storage and sustainable catalysis†

Montu Gogoi,[a] Deepshikha Roy,[a] Jita Morang,[a] Nilakshi Dutta,[a] Tarun Kumar Sahu,[b] Diganta Sarma[a] and Kalyanjyoti Deori*[a]

Rationally constructed lead-free halide perovskite-based composites provide an effective approach for upgrading their many unique physicochemical properties. In this study, we report the design and synthesis of a stable lead-free $CsCu_2I_3$ (CCI) perovskite integrated with g-C_3N_4 (CN) using a simple ultrasonication approach. The individual components, $CsCu_2I_3$ and g-C_3N_4, were synthesized separately using the hot-injection method and the thermal polycondensation method, respectively. Interestingly, the composite material $CsCu_2I_3$@g-C_3N_4 (CCI–CN) exhibited outstanding hybrid supercapacitive behaviour and opened a new avenue for the untapped electrochemical potential of Cu-based lead-free halide perovskites. The hybrid CCI–CN material was also examined, for the first time, as a heterogeneous multifunctional catalyst in the photo-hydration of benzonitrile and the photo-reduction of *para*-nitroaniline. Moreover, the synthesized composite catalyst was very efficient in the synthesis of the medicinally potent N-heterocyclic compounds, quinazolin-4(3*H*)-one moieties. It was observed that $CsCu_2I_3$@g-C_3N_4 not only outperformed its individual components, $CsCu_2I_3$ and g-C_3N_4, but also surpassed other reported catalysts in the aforementioned transformations, delivering excellent product yields. This was attributed to the cooperative and synergistic effects of the $CsCu_2I_3$ and g-C_3N_4 heterojunction. Photoluminescence studies revealed that the reduced recombination in the composite material provided a fast channel for the transfer of photo-generated electrons, with the lower PL lifetime of CCI–CN (119.8307 ns) compared to CCI (151.2798 ns). Hence, this study provides ideas and opportunities of Cu-based halide perovskite composites as efficient materials for charge storage and versatile catalytic activity.

Received 16th May 2025,
Accepted 1st July 2025

DOI: 10.1039/d5qm00374a

rsc.li/frontiers-materials

1. Introduction

Perovskite-based materials have garnered tremendous attention in recent years as emerging candidates for optoelectronic and photovoltaic applications. This is attributed to their remarkable physical and chemical properties, cost-effective manufacturing, and tunable properties.[1,2] Lead-based perovskites are well known and commonly studied for their great potential as semiconductors. However, because of structural instability and lead (Pb^{2+}) ion toxicity, the practical application and commercialization of lead-based perovskite materials are hampered.[3,4] To solve this dilemma of lead-based perovskites, global efforts have been undertaken to develop ecologically acceptable, highly stable and efficient lead-free perovskites. Numerous metals have emerged as potential alternatives to lead, such as Sn^{2+}, Sb^{2+}, Ag^{+}, Bi^{3+}, and Ge^{2+}.[5,6] Above all, copper-based low-dimensional perovskite materials have garnered considerable attention in recent years in the fields of photovoltaic cells, light-emitting diodes (LEDs), and other optoelectronic devices.[7–9] This is attributed to their high photoluminescence quantum yield (PLQY), high thermal and environmental stability, and lower toxicity than Pb^{2+} ions.[10,11] Copper is a readily available, inexpensive and earth-abundant element. Copper is also a good conductor of electricity and serves as a counterpart in various electrical components, which makes it an attractive alternative for perovskite materials.[12] Despite their numerous benefits and emerging applications in different research fields, the activity of Cu-based perovskites in catalysis has not been explored extensively. Hence, using Cu-based perovskite semiconductors as multifunctional heterogeneous catalysts is an effective research hotspot.

[a] *Department of Chemistry, Dibrugarh University, KD's 'NAME' (NanoMat&Energy) Lab, Dibrugarh 786004, Assam, India. E-mail: kalchemdu@gmail.com, kalchemdu@dibru.ac.in*

[b] *Department of Chemistry, Indian Institute of Technology Indore, Madhya Pradesh 453552, India*

† Electronic supplementary information (ESI) available: Kinetics parameters, average lifetime calculation, optimization table of the catalytic reaction, comparison tables, EDX spectra, recyclability test, hot-injection test, ^{1}H and ^{13}C NMR spectra. See DOI: https://doi.org/10.1039/d5qm00374a

To enhance the photocatalytic activity of metal halide perovskites (MHPs), a heterojunction can be constructed with a second semiconductor material to improve the charge transfer mechanism. Graphitic carbon nitride (g-C_3N_4), as a low-cost, environment-friendly and good visible-light-sensitive semiconductor material, has been widely utilized in the development of integrated systems to enhance synergism.[13,14] g-C_3N_4 has a graphene-like 2D layered structure with high physicochemical stability and a medium band gap of approximately 2.7 eV, which has gained abrupt prominence as a photocatalyst.[15] It can be readily synthesized *via* the thermal polycondensation of precursors containing carbon and nitrogen, such as urea, cyanamide, dicyanamide, thiourea and melamine.[16–18]

Amides are ubiquitous as chemical components in the pharmaceutical industry and organic synthesis as well as important constituents of polymeric products.[19,20] Some extensively used medicinal compounds containing amide derivatives are paracetamol, nicotinamide, ranitidine, naropin, and carboxin.[21,22] Moreover, nitriles are usually industrial wastes and are carcinogenic and a threat to environmental integrity.[23] The photocatalytic conversion of toxic benzonitriles to valuable amides is a green and sustainable alternative to the existing harsh approaches for converting harmful chemicals into useful constituents of medicinal and consumer products. Another industrially important reaction is the photocatalytic reduction of *para*-nitroaniline (*p*-NA) to *para*-phenylenediamine (PPD). PPD acts as a versatile intermediate across various industries, including pharmaceuticals, agriculture, and dye manufacturing.[24,25] Many anti-malarial drugs, antibacterial agents and other therapeutic compounds contain PPD as a major intermediate.[26,27] Nitro-compounds are also hazardous industrial effluents, and the reduction of these harmful compounds *via* a green pathway is beneficial for the environment.

Except for a few literature studies employing Cu-based perovskites as catalysts in organic reactions, there is not a single report available showcasing their ability in the field of medicinal research. Hence, in addition to the photocatalytic hydration of benzonitrile and reduction of *para*-nitroaniline, we wanted to test the potential of our as-synthesized catalyst in the synthesis of one of the medicinally potent N-heterocyclic compounds, quinazolin-4(3*H*)-ones. These are vital components in numerous medicines, including those exhibiting anti-cancer, antimalarial, anti-inflammatory, anti-tumor, anti-diabetic, dihydrofolate reductase inhibitory, and kinase inhibitory activities.[28–30] Quinazolinones are the winning horse in drug discovery, having served as a stepping stone toward more than 150 naturally occurring alkaloids isolated from different microorganisms, plants, and animals. Quinazolinones are of utmost importance in the current research scenario because of their attractive physicochemical properties, lipophilicity and stability.[31,32]

Perovskite materials are well known for their energy applications. If a sustainable material can not only support multifunctional catalytic applications but also address the growing demand for sustainable energy solutions, it will undoubtedly gain greater prominence in today's scientific research landscape. While several sustainable electrochemical processes, such as fuel cells, water splitting, batteries and supercapacitors, have emerged as green energy solutions to combat the global energy crisis, the search for new and alternative energy materials for diverse electrochemical applications remains ongoing.[33–35] Among these, supercapacitors have garnered significant attention as energy storage devices owing to their superior power and energy density and longer life cycle compared to traditional dielectric capacitors and batteries.[36,37]

Hence, keeping these observations in mind, we developed a non-toxic, stable and lead-free Cu-based perovskite, $CsCu_2I_3$ (CCI), coupled with g-C_3N_4 (CN) and denoted as $CsCu_2I_3$@g-C_3N_4 (CCI–CN). This composite material was prepared using an ultrasonication method. As observed in some previous studies, we expected a favourable band alignment between the two semiconductor materials, leading to improved charge carrier dynamics.[38–41] Yixuan Lv *et al.* synthesized $CsCu_2I_3$/g-C_3N_4 and studied its photocatalytic efficiency for generating H_2 *via* hydroiodic acid (HI) splitting.[42] However, the multifunctional behaviour of this material is still underexplored. To reveal its further potential not only in catalysis, we explored the energy application of our as-synthesised CCI–CN composite. Interestingly, the as-synthesized CCI–CN demonstrated exceptional hybrid supercapacitive behaviour, which opens numerous exciting avenues for further in-depth exploration of the untapped electrochemical potential of the Cu-based lead-free halide perovskite. To the best of our knowledge, no studies have been reported on the use of $CsCu_2I_3$-based materials for energy storage applications. The as-synthesized CCI–CN composite exhibited excellent catalytic efficiency in the photo-hydration of benzonitriles to benzamide, photo-reduction of *para*-nitroaniline to *para*-phenylenediamine and synthesis of quinazolin-4(3*H*)-ones with excellent yields. Moreover, the exploration of multifunctional heterogeneous catalysis using the Cu-based perovskite and its supercapacitive behaviour is still in its infancy. Our study demonstrates the potential of the Cu-based perovskite composite $CsCu_2I_3$@g-C_3N_4 in catalyzing important organic reactions and as a modern sustainable energy storage device.

2. Experimental section

2.1. Materials

Caesium carbonate (Cs_2CO_3, 98%), 2-aminobenzamide (98%), *para*-nitroaniline, oleylamine (OAm), benzaldehyde, benzonitrile and all related substrates were purchased from TCI. Copper iodide (CuI, 99.5%), dimethyl sulfoxide (DMSO; 99%) and sodium borohydride ($NaBH_4$, 95%) were purchased from MERCK. Oleic acid (OA), octadecene (ODE) and Nafion were purchased from Sigma-Aldrich. Isopropanol (i-PrOH, 99.5%), potassium hydroxide (KOH) and melamine were supplied by SRL. Thin-layer chromatography was performed using silica-gel 60F_{254} plates and checked under UV light. The obtained products were isolated by column chromatography over silica gel (60–120 mesh). All chemicals were used as received for this study without further purification.

2.2. Characterization

Powder X-ray diffraction (PXRD) patterns were obtained by using monochromatic Cu Kα radiation (λ = 1.54056 Å) on a

Bruker D8 Advance X-ray diffractometer. X-ray photoelectron spectroscopy (XPS) measurements were performed using a Thermo Fisher ESCALAB Xi^+ electron spectrometer. All binding energy values were calibrated with reference to the C 1s peak (284.6 eV). Scanning electron microscopy (SEM) imaging, energy-dispersive X-ray spectroscopy (EDX), and elemental mapping measurements were performed on a JEOL model JSM-7900F scanning electron microscope. Low-magnification transmission electron microscopy (TEM) images, high-resolution TEM (HRTEM) images, and selected area electron diffraction (SAED) patterns were obtained using a JEM-2100 Plus transmission electron microscope operating at 200 kV. The surface areas and pore sizes of the as-synthesized samples were determined using the multipoint Brunauer–Emmett–Teller (BET) equation with the help of a Quantachrome Autosorb iQ_2 instrument from Aton Paar at 77 K. The UV-visible absorption spectra were collected on a Shimadzu UV-1700 UV-visible spectrophotometer. The photoluminescence (PL) spectra were analyzed using the Horiba Scientific Fluoromax-4C spectrophotometer. Thermogravimetric analysis (TGA) tests were conducted on a Mettler Toledo TGA/DSC 1 STARe analyzer. A Bruker Ascend 500 MHz spectrophotometer was used to collect ^1H and ^{13}C NMR spectra at 500 MHz and 125 MHz, respectively.

2.3. Synthesis of the Cs-oleate (CsOA) precursor

The CsOA precursor was synthesized *via* a reported route.[43] Briefly, Cs_2CO_3 (1 mmol), OA (2 mL), and ODE (10 mL) were added to a two-neck round-bottom flask, and the mixture was stirred for 60 minutes at 120 °C under vacuum conditions. A transparent solution of the CsOA precursor was obtained. Then, the as-obtained CsOA precursor was kept at 100 °C in an N_2 atmosphere for the subsequent synthesis of $CsCu_2I_3$.

2.4. Synthesis of $CsCu_2I_3$

The lead-free Cu-based halide perovskite $CsCu_2I_3$ was synthesized following a hot-injection method and denoted as CCI. Briefly, CuI (2 mmol), OAm (1.5 mL), OA (0.5 mL), and ODE (10 mL) were taken in a two-neck flask (100 mL). The resulting mixture was stirred at 120 °C for 60 min under vacuum conditions. After the reactants were dissolved, the reaction mixture was heated to 150 °C in an N_2 environment. Subsequently, 6 mL of the as-prepared CsOA precursor solution was quickly injected into the two-neck flask, and the precipitate of CCI was formed in no time. After letting the reaction proceed for 5 minutes, an ice-water bath was used to reduce the reaction temperature, and the required perovskite was obtained. After centrifugation, the as-obtained perovskite products were washed several times with *n*-hexane. Finally, the collected perovskite samples were dried in an oven at 65 °C for 24 h for further characterization.

2.5. Synthesis of $CsCu_2I_3$@g-C_3N_4

Polymeric g-C_3N_4 was prepared by the thermal polycondensation of melamine.[44] For the synthesis of the $CsCu_2I_3$@g-C_3N_4 heterojunction, briefly, 50 mg of the as-prepared g-C_3N_4 powder was dispersed in an appropriate volume of *n*-hexane and ultrasonicated for 15 min. Subsequently, a specific amount of $CsCu_2I_3$ was added to the above-mentioned mixture and subjected to ultrasonication for 30 min. Finally, the resulting composite material was obtained by centrifugation, followed by drying at 65 °C. The as-prepared composite sample was denoted as CCI–CN.

2.6. Photocatalytic measurements

Photocatalytic measurements were performed in a photocatalytic reactor equipped with a 7 W and 250 W visible light source with a wavelength distribution range of 400–700 nm. The distance between the reaction tubes placed on a magnetic stirrer and the light source was about 6 cm. The temperature of the illuminated photoreactor was maintained between 27 °C and 30 °C throughout the reaction using a cold-water-circulating tank attached to the reactor.

2.7. Electrode fabrication and electrochemical measurements

In brief, the working electrode was fabricated by dissolving the as-synthesized composite material (5 mg) in a solution containing iso-propanol (100 μL) and Nafion (20 μL), followed by sonication for 60 min to obtain a well-dispersed suspension. Then, 10 μL of this suspension was drop-cast onto the surface of a glassy-carbon electrode (GCE) with a 3-mm diameter and dried at room temperature overnight in a desiccator.

All electrochemical measurements were carried out using a CHI760E electrochemical workstation consisting of a conventional three-electrode system with the glassy carbon electrode (GCE) as a working electrode in 0.5 M H_2SO_4 at room temperature ($\sim$25 °C). A Pt electrode and an Ag/AgCl electrode were used as the counter and reference electrodes, respectively. Cyclic voltammetry (CV) and galvanostatic charge–discharge (GCD) curves at various scan rates and current densities were recorded, respectively, in the potential window from −0.3 to 0.3 V to evaluate the supercapacitive behavior of the as-synthesized material. Electrochemical impedance spectroscopy (EIS) spectra were also recorded at the open-circuit potential (OCP) in the frequency range of 0.001–1000 Hz using the AC voltage with an amplitude of 5 mV to evaluate the solution and charge-transfer resistance.

2.8. Photocatalytic hydration of benzonitrile

The photocatalytic hydration of benzonitrile using the synthesized Cu-based perovskite heterojunction was carried out under the continuous irradiation of visible light. In a photocatalytic reaction tube, benzonitrile (0.5 mmol), potassium hydroxide (KOH, 1 mmol), isopropanol (2.5 mL), and the photocatalyst (10 mg) were mixed, and the resulting mixture was stirred under continuous uninterrupted irradiation of 250-W visible light at room temperature. The progress of the reaction was monitored by the TLC method (*n*-hexane/ethyl acetate) under UV light. After the completion of the reaction, a workup procedure was performed, and the catalyst was recovered by centrifugation. The final products were isolated using column chromatography over silica gel (60–120 mesh) and characterized by ^1H and ^{13}C NMR using DMSO as the solvent for NMR sampling.

2.9. Photocatalytic reduction of *para*-nitroaniline

To test the efficiency of our synthesized material in photocatalytic *para*-nitroaniline reduction, an aqueous solution of *para*-nitroaniline (50 mL, 20 mg L^{-1}) and sodium borohydride ($NaBH_4$, 5 mg) were taken in a round-bottom flask. To this mixture, the photocatalyst (10 mg) was added, and the reaction mixture was placed in a reaction chamber under 7-W visible light. The progress of the reaction was monitored using UV-visible spectroscopy in the wavelength range of 250–600 nm.

2.10. Synthesis of quinazolin-4(3*H*)-ones

The viability of the as-synthesized composite was tested in the synthesis of 2-phenylquinazolin-4(3*H*)-one derivatives. Briefly, 2-aminobenzamide (0.1 mmol, 1 equivalent) and benzaldehyde (0.12 mmol, 1.2 equivalent) were taken in an oven-dried round-bottom flask. Dimethyl sulfoxide (DMSO) (1 mL), as the solvent, and the catalyst (10 mg) were added to this mixture. The reaction mixture was stirred under refluxed conditions at 80 °C for 4 h in air. The progress of the reaction was monitored by TLC under UV irradiation. After the completion of the reaction, the reaction mixture was allowed to cool, and the catalyst was recovered. Column chromatography was used for the purification of the obtained products, which were identified by ^1H and ^{13}C NMR using DMSO as the solvent for NMR sampling.

3. Results and discussion

3.1. Composition, purity, morphology and optical properties of the As-synthesized CCI and CCI–CN

The $CsCu_2I_3$@g-C_3N_4 (CCI–CN) composite was prepared by employing a simple ultrasonication approach using $CsCu_2I_3$ (CCI) and g-C_3N_4 (CN). The individual components, $CsCu_2I_3$ and g-C_3N_4, were synthesized separately using hot-injection and thermal polycondensation methods, respectively (Scheme 1).

The crystalline phase of the as-synthesized $CsCu_2I_3$@g-C_3N_4 (CCI–CN) composite was confirmed using powder X-ray diffraction (XRD) patterns (Fig. 1(a)). The material evidently exhibits the diffraction pattern of $CsCu_2I_3$ (CCI), with main peaks at 2θ of 21.6°, 26.2°, 27.1°, 29.2°, 33.9°, 40.3°, and 44.05° well-assigned to the diffraction of the (220), (221), (040), (002), (202), (042), and (242) planes of orthorhombic $CsCu_2I_3$ (PDF# 77-0069, space group = *Cmcm*), respectively. The main characteristic peak of g-C_3N_4 (CN) is close to that of CCI at 27°, corresponding to the (040) crystal plane of CCI, and it does not produce any extra crystalline diffractions. The alignment of the characteristic diffraction patterns of CN and CCI at 27° suggests a comparable interplanar distance and leads to the overlapping of the diffraction patterns at 27°. The overlapping of the peaks indicates a high degree of compatibility at the interface, which is beneficial for photocatalysis.[45] The absence of any unnecessary peaks in the XRD profiles corroborates the phase purity of the sample and the preservation of the intrinsic crystalline properties of CCI and CN.

To confirm the amalgamation of CN with CCI without altering the bulk crystallinity of the composite, we performed FTIR analysis. FTIR can provide complementary information about the surface-level interactions that do not alter the crystal structure.[46] The FTIR spectrum in Fig. 1(b) explains the presence of the characteristic peaks of CN in the composite CCI–CN. The broadening of the N–H stretching band in CCI–CN suggests a significant interfacial interaction between the participating counterparts.

The morphologies and elemental distributions of the samples were monitored by scanning electron microscopy (SEM), transmission electron microscopy (TEM), and energy-dispersive X-ray spectroscopy (EDX) mappings (Fig. 1(c), (d), 2(a)–(f), 3(a)–(h) and Fig. S1a, ESI†). As shown in Fig. 1(c) and (d), the morphology of the CCI perovskite appears to be rod-shaped with sharp edges and that of CCI–CN appears to be somewhat different from the parent rod-shaped morphology. The incorporation of g-C_3N_4 disrupts the growth and alignment of CCI rods, leading to a

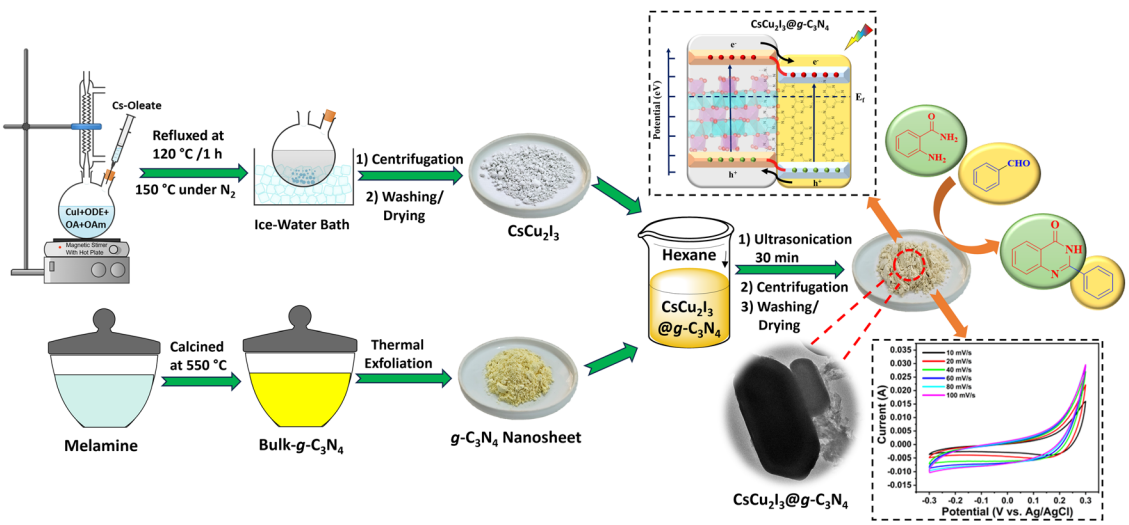

Scheme 1 Schematic of the synthesis of the $CsCu_2I_3$@g-C_3N_4 (CCI–CN) composite material and its potential applications.

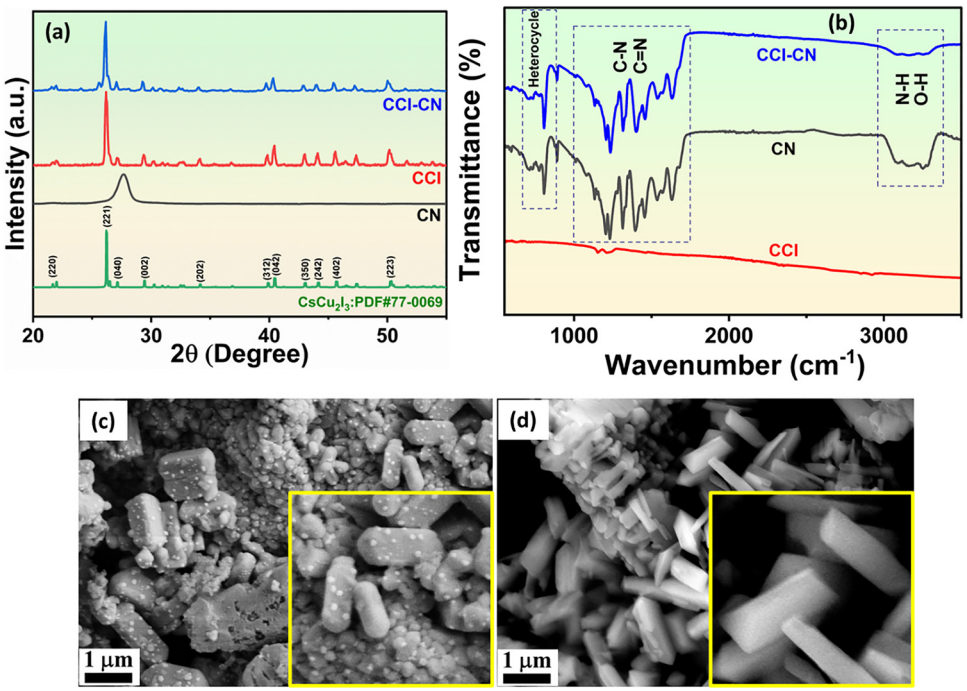

Fig. 1 (a) PXRD patterns of CCI–CN (blue), CCI (red), and CN (black); (b) FTIR spectra of CCI–CN (blue), CCI (red), and CN (black); and SEM images of (c) CCI–CN and (d) CCI.

significant change in their morphology, and this change can increase the exposed surface area and number of active sites available for photocatalysis.[47] In the SEM image of the $CsCu_2I_3$@g-C_3N_4 composite (Fig. 1(c)), the characteristic sheet-like morphology of g-C_3N_4 is not distinctly visible, which may be attributed to its surface coverage and encapsulation by $CsCu_2I_3$ nanocrystals during composite formation. Additionally, the poor visibility of the g-C_3N_4 morphology may result from its ultrathin nature, making it difficult to resolve clearly during SEM imaging.

The TEM images of CCI and CCI–CN at different magnifications are depicted in Fig. 2, where the morphological changes from CCI to CCI–CN can be clearly identified. Bare CCI exhibits a rod-shaped morphology with a uniform elemental distribution (Fig. 2(a)). The disruption and change in the morphology

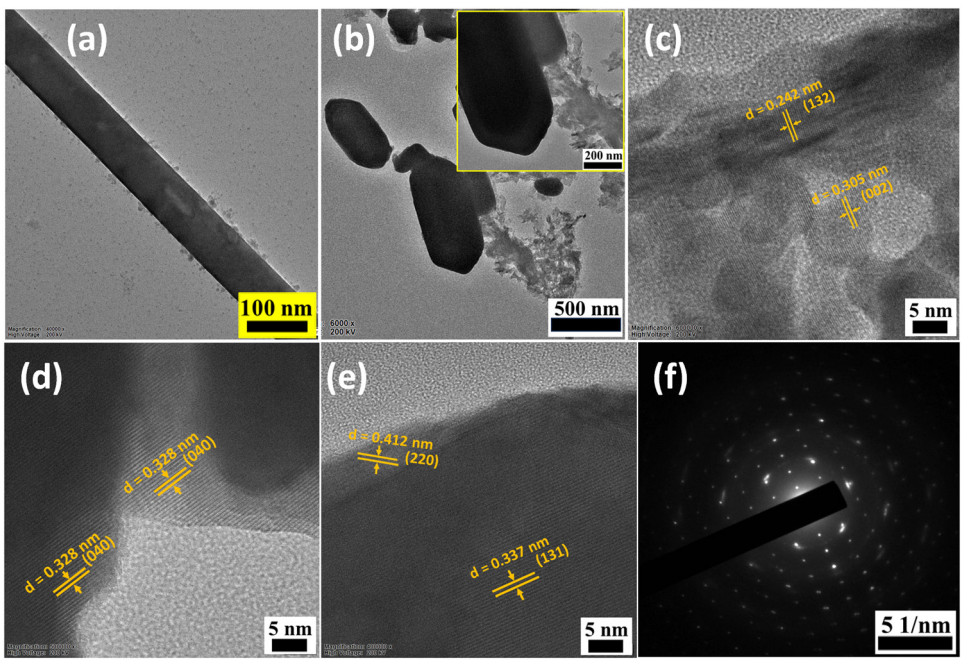

Fig. 2 TEM images of the (a) CCI and (b) CCI–CN; (c)–(e) crystal fringes in different regions of the CCI–CN and (f) SAED pattern of the CCI–CN.

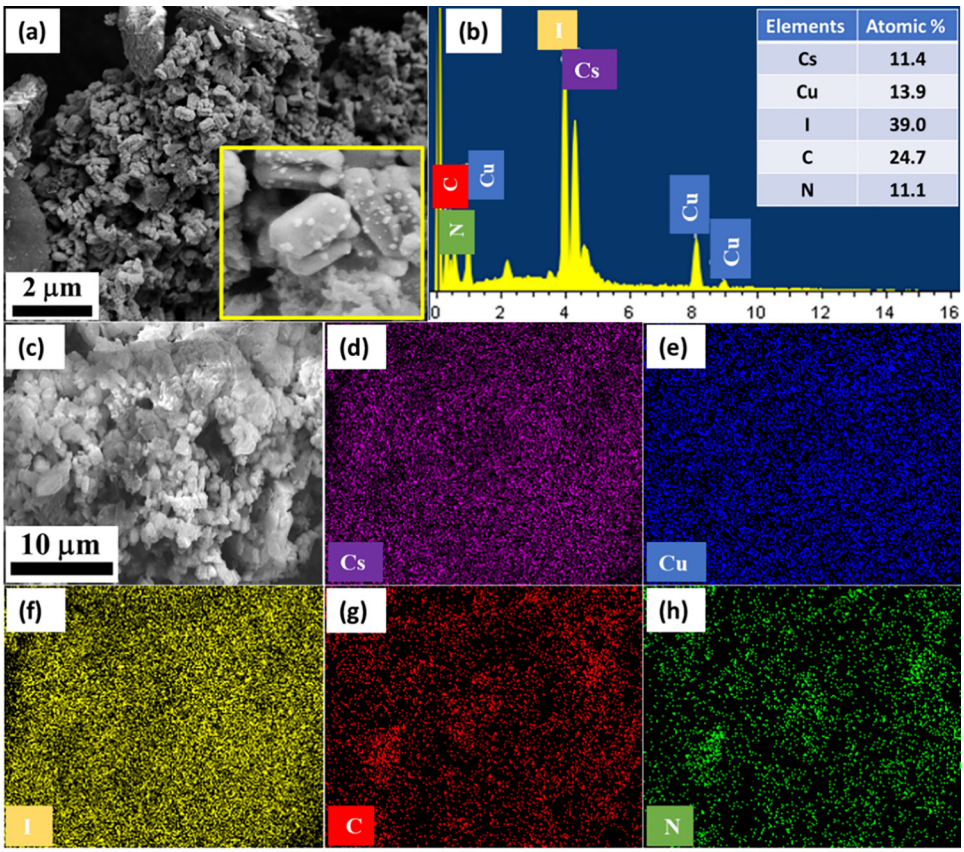

Fig. 3 (a) SEM image, (b) EDX spectrum, and (c)–(h) elemental mapping images of the constituent elements of the CCI–CN.

of CCI–CN are displayed in Fig. 2(b). High-resolution TEM (HRTEM) images (Fig. 2(c)–(e)) show the clear lattice fringes of CCI–CN, with *d*-spacings of 0.242, 0.305, 0.328, 0.412, and 0.337 nm, corresponding to the (132), (002), (040), (220), and (131) planes, respectively. Due to their semi-crystalline nature, CN layered sheets exhibit a less noticeable lattice fringe. The SAED pattern of CCI–CN in Fig. 2(f) displays distinct diffraction spots, confirming its high crystallinity. In summary, the TEM images and element mappings of CCI–CN confirm the successful encapsulation of $CsCu_2I_3$ and g-C_3N_4.

The elemental composition of the as-synthesized samples, examined by EDX spectroscopy, confirms the presence of all expected elements for CCI–CN (C, N, Cu, I, and Cs) and CCI (Cu, I, and Cs) (Fig. 3(b) and Fig. S1b, ESI†). Furthermore, the elemental mapping of the samples indicates the uniform distribution of all constituents across the CCI–CN (Fig. 3(c)–(h)) and CCI (Fig. S1c–f, ESI†) structures.

The UV-visible spectra were recorded to examine the light-harvesting characteristics of the as-prepared perovskite samples. The resulting spectra in Fig. 4(a) and Fig. S2a (ESI†) reveal that the samples are UV- and visible light-responsive, with a broad absorption tail in the visible region. Compared to CCI, the absorption capacity of the CCI–CN composite broadens toward the visible region because of the introduction of g-C_3N_4 (CN), which enhances the absorption intensity. By employing Tauc's method, the corresponding band gap energies of the samples were determined. The band gap energy of CCI–CN is measured to be 3.03 eV, CCI is 3.49 eV (Fig. 4(a)) and CN is 3.16 eV (Fig. S2a, ESI†). The alignment of the conduction band (CB) and valence band (VB) levels of CCI with those of CN may result in band edge shifting, narrowing the effective band gap of the CCI–CN composite. The as-obtained band gap energies are in good agreement with the standard $CsCu_2I_3$ (CCI), which supports the observed photocatalytic activity of CCI–CN under visible light irradiation.[48]

The radiative recombination process of photo-excited charge transfer in photocatalysts can be detected using the photoluminescence (PL) emission spectra (Fig. 4(b) and Fig. S2b, ESI†). The diminished PL intensity of CCI–CN at an excitation wavelength of 330 nm, compared to its counterpart CCI, reveals that the composite sample has reduced charge recombination and better photo-generated carrier separation. This explains the enhanced photocatalytic activity of CCI–CN compared to its counterparts. The time-resolved PL decay curves of CCI and CCI–CN are shown in Fig. 4(c). The decay profiles of the composite can be fitted with a biexponential decay function (eqn (1)).

$$I_t = I_0 + A_1 \exp\left(-\frac{t}{\tau_1}\right) + A_2 \exp\left(-\frac{t}{\tau_2}\right) \quad (1)$$

where I_0 and I_t are the initial luminescence intensity and intensity at time t, respectively, and τ_1 and τ_2 are the lifetimes of the exponential components, respectively. A_1 and A_2 are constants.

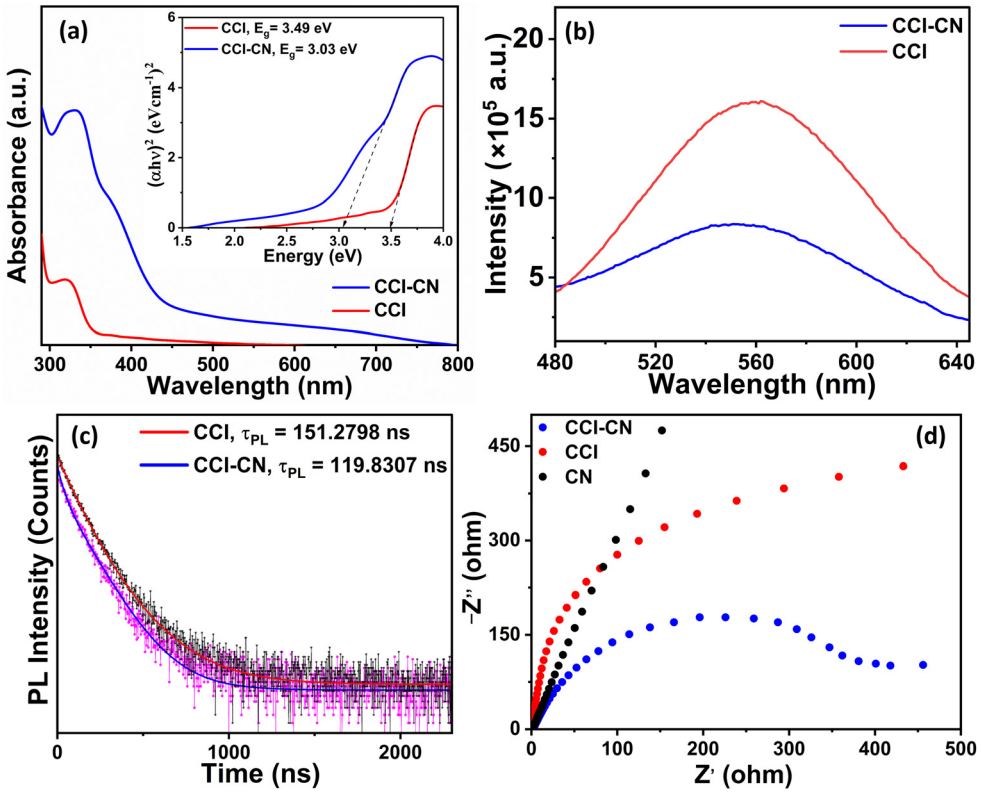

Fig. 4 (a) Absorption spectra. The inset shows the corresponding band gap energies of the samples using the Tauc plot. (b) PL emission spectra of the CCI and CCI–CN. (c) Time-resolved PL decay curves of the CCI and CCI–CN. (d) EIS spectra of the CCI–CN, CCI, and CN.

The average lifetime was calculated using eqn (S5) (ESI†), which shows an obvious decrease from 151.2798 ns to 119.8307 ns after composite formation. The PL quenching and average lifetime decreases of CCI–CN compared to that of CCI confirm efficient charge transfer and separation in the CCI–CN composite. As shown in Fig. S2c (ESI†), the slower decay of CCI–CN than that of pristine CN can be attributed to the Coulombic repulsion of electrons injected under excitation from the conduction band of CCI to the partially filled conduction band of CN.[49] A summary of the kinetic parameters is presented in Table S1 (ESI†).

Electrochemical impedance spectroscopy (EIS) (Fig. 4(d)) reveals that the optimal sample CCI–CN has a smaller semicircle, *i.e.*, minimum impedance, than the counterparts CCI and CN, which indicates that the resulting composite has a higher charge transfer capability. This explains that the formation of the heterojunction accelerates the transfer of photogenerated charge carriers in the composite, proving the enhanced photocatalytic activity of the as-synthesized composite compared to the individual counterparts.

The XPS survey spectra and relative high-resolution spectra were obtained to reveal the surface composition and chemical states of the as-synthesized composites. The peak positions of CCI were ascribed by comparing its binding energy to the XPS database. In CCI, the Cs 3d peaks at 738.42 and 724.45 eV correspond to $3d_{3/2}$ and $3d_{5/2}$, respectively (Fig. 5(a)). The spin–orbital component of these two substantial peaks is separated by 14.06 eV. The characteristic peaks of Cu ($2p_{1/2}$ = 951.3 eV and $2p_{3/2}$ = 931.3 eV, D = 20 eV) and I ($3d_{3/2}$ = 630.8 eV and $3d_{5/2}$ = 619.3 eV, D = 11.5 eV) in the synthesized CCI sample match with those reported in the literature, demonstrating the purity of the sample (Fig. 5(b) and (c)).[50–52] In contrast to CCI, the binding energies of Cu 2p in CCI–CN shift to higher binding energies ($2p_{1/2}$ = 953.4 eV and $2p_{3/2}$ = 933.4 eV), maintaining the peak difference of 20 eV (Fig. 5(b)). This shift in the peak position indicates the presence of an electron transfer mechanism between $CsCu_2I_3$ and g-C_3N_4 in the CCI–CN composite. Distinguished peaks for the C 1s and N 1s of g-C_3N_4 with a slight peak shift or broadening are observed in CCI–CN (Fig. 5(d) and (e)). The XPS survey spectra of g-C_3N_4, CCI, and CCI–CN are displayed in Fig. 5(f). Thus, the confirmation of the synergistic effects of $CsCu_2I_3$ and g-C_3N_4 was gained by comparing the XPS peaks of Cs, Cu, and I in $CsCu_2I_3$ and $CsCu_2I_3$@g-C_3N_4.

To investigate the specific surface areas and porosities of the samples, isothermal N_2 adsorption–desorption measurements at 77 K were performed (Fig. 6(a)–(c)). The measured Brunauer–Emmett–Teller (BET) surface areas of CCI, CCI–CN and CN samples are calculated to be 5.321, 6.83 and 2.053 $m^2\ g^{-1}$, respectively. The average pore diameter is found to be 3.064 nm for CCI and 3.437 nm for CCI–CN. The increase in the pore size and surface area of CCI–CN may lead to the easier diffusion of larger reactants into the active sites of CCI–CN during catalytic applications. The thermal stability of the as-synthesized CCI–CN sample was characterized by TGA (Fig. 6(d)). The analysis was performed in a temperature range from 25 to 815 °C in an

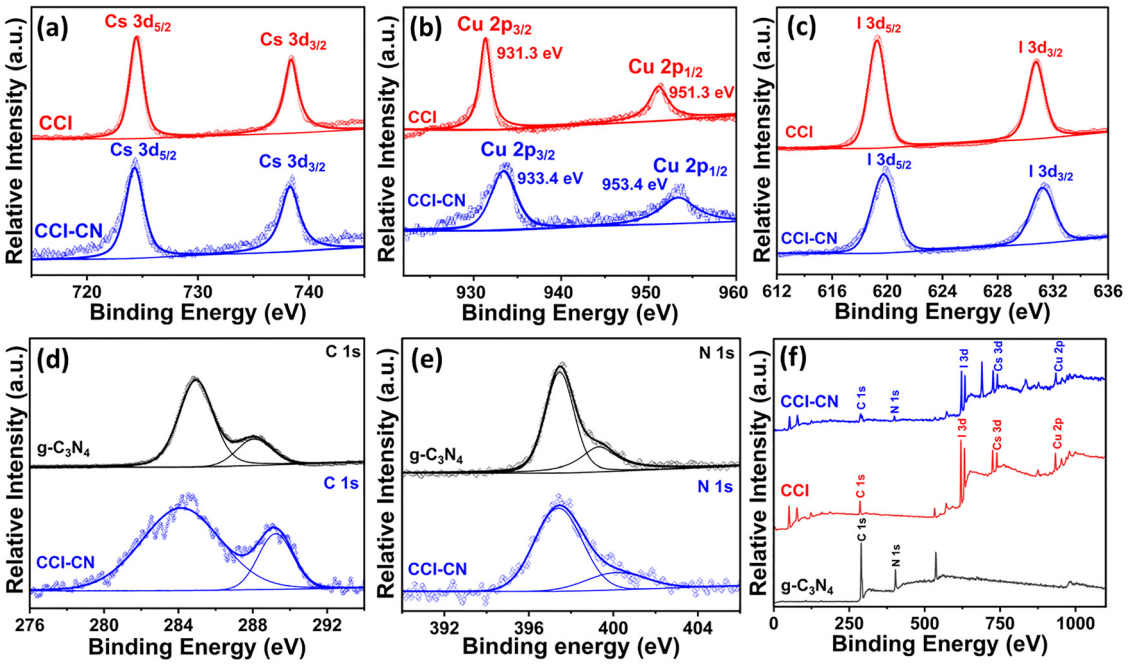

Fig. 5 High-resolution XPS spectra for (a) Cs 3d, (b) Cu 2p, (c) I 3d, (d) C 1s, and (e) N 1s of the CCI and CCI–CN. (f) XPS survey spectra of the CCI–CN, CCI, and g-C_3N_4 (CN).

inert N_2 atmosphere. The synthesized CCI–CN sample exhibits a multistage decomposition pattern. A temperature-dependent weight loss for CCI–CN is observed at 400–500 °C, indicating the high thermal stability of the composite.

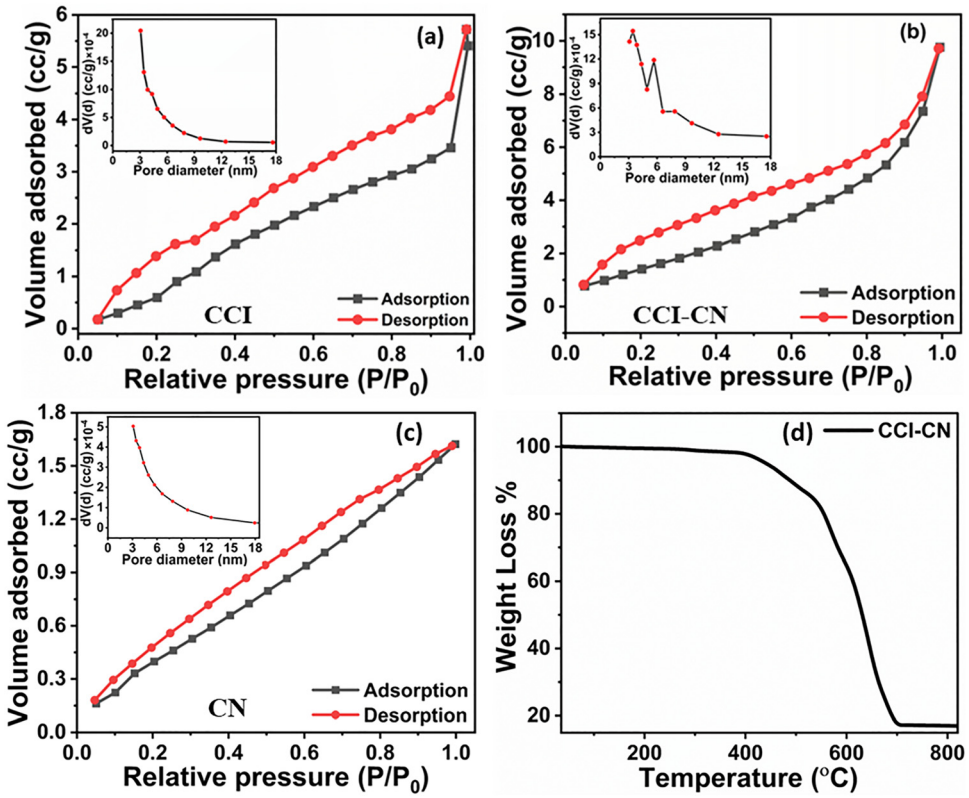

Fig. 6 N_2 adsorption–desorption isotherms of the (a) CCI, (b) CCI–CN, and (c) CN at 77 K. Insets show the respective pore size distribution graphs between the pore volume distribution and the pore diameter. (d) TGA graph of the CCI–CN.

3.2. Catalytic properties

In this study, the catalytic performance of the as-synthesized CCI–CN composite was evaluated in the photo-hydration of benzonitriles to corresponding benzamide derivatives, which are intermediates in organic synthesis, pharmaceuticals, polymeric consumer products, *etc.* The primary screening of the reactions was performed using benzonitrile (**1a**) as the model substrate. It revealed that the most suitable conditions were achieved when 2.5 mL of i-PrOH was used as the solvent, 1 mmol KOH as the base, and 10 mg of CCI–CN as the photocatalyst under continuous 250-W visible light irradiation.

Under similar reaction conditions, CCI–CN showed superior photocatalytic activity over its individual components and was chosen for optimizing different reaction variables (Table S2 entries 4 and 5, ESI†). The reaction did not proceed forward in the absence of either light or the catalyst (Table S2 entries 2 and 3, ESI†). Isopropanol was found to be the most suitable solvent, outperforming other solvents such as MeOH, EtOH and H_2O, which can be attributed to its balanced polarity that can effectively solubilize the organic reactant and intermediate species formed during the reaction (Table S2 entries 6–8, ESI†). Isopropanol is also known to be an excellent hole scavenger, which, upon interacting with photo-generated holes, can effectively reduce the recombination rates and enhance the catalytic efficiency.[53] Likewise, KOH was found to be the most suitable base for this reaction. Apart from the base and solvent, the power of the light source also influenced the photocatalytic result. Replacing 250-W visible light with 20-W visible light resulted in decreased reaction yields due to lower electron–hole pair generation, slower reactant activation and other related factors (Table S2 entry 9, ESI†). Decreasing the amount of the photocatalyst from 10 to 5 mg lowered the product yield from 97% to 81% (Table S2 entry 13, ESI†).

Finally, the optimal condition, as mentioned above, was chosen for investigating the substrate scope (Table 1). The nitrile substrates with electron-withdrawing groups (EWGs) at the *para* position, *i.e.* *p*-Cl, *p*-I, *p*-CN, and *p*-NO_2, showed excellent yields of the corresponding amides (Table 1, entries **2b**, **2c**, **2h**, and **2j**). However, nitrile substituents having electron-donating groups (EDGs) at the *para* position, *i.e.* *p*-CH_3 and *p*-OCH_3, exhibited a poor benzamide product yield (Table 1, entries **2d** and **2e**). EDGs at the *para* position reduce the electrophilicity of the nitrile carbon by donating an electron density to the nitrile group, making it less susceptible to a nucleophilic attack. This decrease in the electrophilicity of the nitrile group may slow the formation of the imine intermediate and lead to a lower yield of benzamide. Upon comparing with the existing literature, our as-synthesized photocatalytic system was found to be very efficient and eco-friendly for the synthesis of benzamide derivatives without involving high-temperature and -pressure additives (Table S4, ESI†).

Next, we tested the efficiency of our as-synthesized CCI–CN catalyst in the photo-reduction of *para*-nitroaniline (*p*-NA) to the corresponding *para*-phenylenediamine (PPD) under the irradiation of 7-W visible light. The reduction of *p*-NA was monitored *via* optical measurement studies at different time intervals (Fig. 7(a)). Without the illumination of light, *p*-NA exhibited a strong absorption band at around 380 nm. A blank experiment was carried out by only illuminating the *p*-NA solution with light without using the catalyst. No significant reduction in the absorbance peak was observed at 380 nm, showing the importance of the catalyst (Fig. S3, ESI†). A similar result was obtained when the reaction was carried out under dark conditions in the presence of the CCI–CN catalyst (Fig. S3, ESI†). CCI and CN only as catalysts exhibited much lower efficiency in *p*-NA reduction than CCI–CN (Fig. 7(b)). As shown in Fig. 7(a), the introduction of CCI–CN under 7-W visible light irradiation significantly decreased the absorption peak of *p*-NA at a wavelength of 380 nm, with the concomitant increase in the absorption peak at around 300 nm corresponding to PPD (Fig. 7(a)). Physically, the change in the colour of the aqueous *p*-NA solution from yellow to colourless also clearly indicated the subsequent reduction of *p*-NA (inset image in Fig. 7(c)). Using a pseudo-first-order kinetics, a quantitative comparison of the rate constant (k) was performed. An excellent photocatalytic reduction efficiency of 96% (eqn (2)) was obtained for CCI–CN with a rate constant of 0.25 min^{-1} (eqn (3)), which outperforms the catalytic efficiencies (~68%) of CCI and (~39%) CN, with rate constants of 0.11 and 0.04 min^{-1}, respectively.

$$\text{Photocatalytic reduction efficiency}\,(\%) = \left(\frac{C_0 - C_t}{C_0}\right) \times 100 \quad (2)$$

$$\ln(C_0 - C_t) = kt \quad (3)$$

where C_0 is the initial absorbance, C_t is the absorbance at time t, and k is the rate constant.

Table 1 Substrate scope of the CCI–CN for the photo-hydration of benzonitrile to the corresponding benzamide derivatives[a]

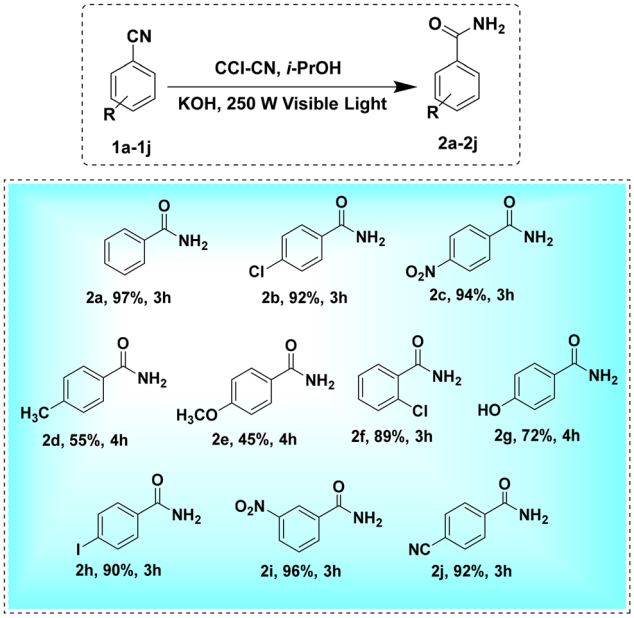

[a] Reaction conditions: benzonitrile (0.5 mmol), KOH (1 mmol), and the CCI–CN (10 mg) were stirred in i-PrOH (2.5 mL) under 250-W visible light irradiation. All yields are reported as isolated yields.

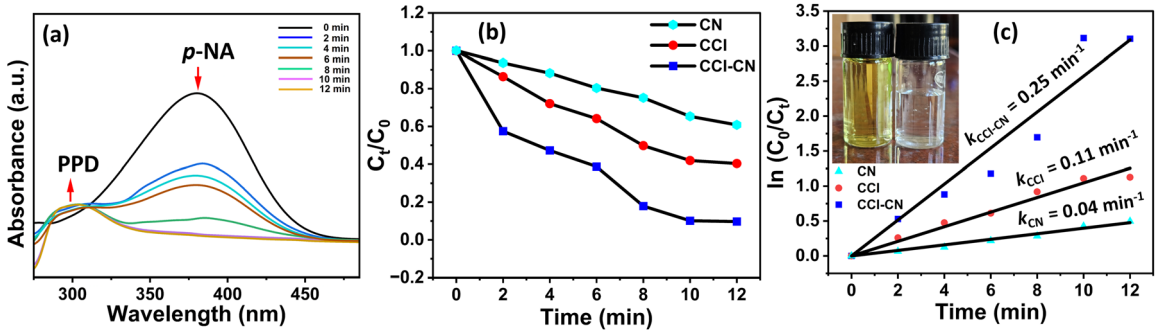

Fig. 7 (a) Time-dependent optical absorption spectra for the *p*-NA reduction using the CCI–CN; (b) comparison of the photocatalytic efficiencies of the CN, CCI and CCI–CN; and (c) kinetic plots for the photo-reduction of a *p*-NA solution using the CCI–CN under visible light irradiation.

The interfacial heterojunction formed between $CsCu_2I_3$ and g-C_3N_4 facilitates charge transport and promotes the effective separation of photo-generated electron–hole pairs. This significantly reduces the charge recombination compared to that in the individual components, which is also evident from our above-mentioned analysis (PL and EIS spectra). The electrons are transferred from the conduction band of $CsCu_2I_3$ to the conduction band of g-C_3N_4, and the counterpart g-C_3N_4 serves as trap sites for electrons and fuels the reduction in the recombination process. The composite exhibits an enhanced visible light absorption and hence a decreased overall band gap compared to that in $CsCu_2I_3$, in which g-C_3N_4 acts as the photosensitizer to enhance light absorption. The reduced recombination rate of electrons and holes lowers their potential energy and prolongs their lifetime.

The plausible reaction pathways for the photo-hydration of benzonitrile to the corresponding benzamide and the photo-reduction of *para*-nitroaniline (*p*-NA) to *para*-phenylenediamine (PPD) are shown in Fig. 8(a) and (b), respectively. The photo-generated electrons from the heterogeneous $CsCu_2I_3$@g-C_3N_4 catalyst facilitate the conversion of *p*-NA to the hydroxylamine intermediate (–NHOH). The hydride ion (H^-) released from $NaBH_4$ plays a crucial role in the reduction of the hydroxylamine intermediate to produce PPD. In the case of photocatalytic benzonitrile hydration, the photo-generated electron activates the benzonitrile substrate and subsequent nucleophilic attack of the OH^- ion generated from KOH, resulting in the formation of the imine intermediate. The rearrangement of this intermediate yields the corresponding benzamide.

Furthermore, to justify the viability and feasibility of our as-synthesized CCI–CN catalyst, we designed a sustainable protocol to synthesize one of the medicinally potent N-heterocyclic compounds, quinazolin-4(3*H*)-ones, following a condensation-cyclization pathway using 2-aminobenzamide and benzaldehyde. To achieve the optimal conditions, a series of reactions were performed considering 2-aminobenzamide (**3a**) and 4-methylbenzaldehyde (**4b**) as the model substrates. The reaction resulted the best yield of the targeted product at 80 °C in air for 4 h. Using H_2O as the solvent resulted in a 50% yield of quinazolin-4(3*H*)-one, and after replacing H_2O with DMSO, the product yield effectively increased up to 98% (Table S3 entry 4, ESI†). The reaction did not proceed efficiently in methanol and ethyl acetate, presumably because of the poor solubility of the substrates in the respective solvents (Table S3 entries 5 and 6, ESI†). From the screening of solvents, DMSO was found to be the best solvent for this protocol. The optimization of the reaction temperature revealed that the

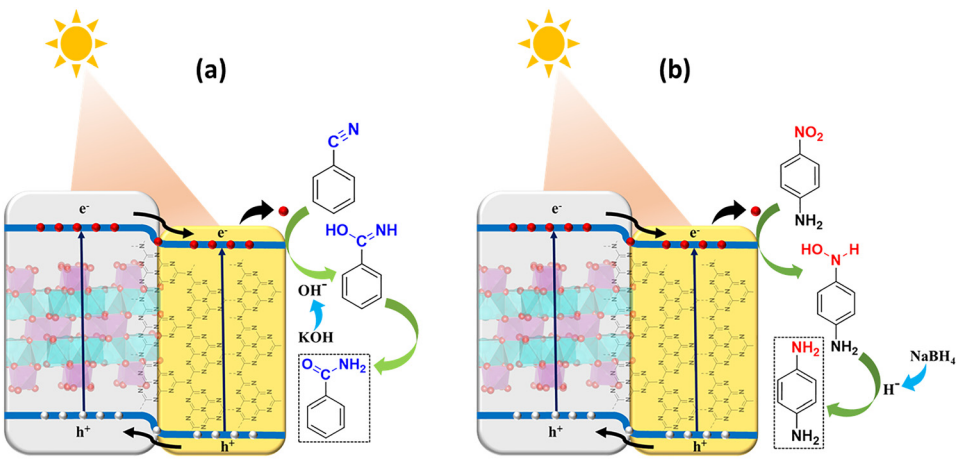

Fig. 8 Plausible mechanisms for the photocatalytic (a) hydration of benzonitrile to benzamide and (b) reduction of *para*-nitroaniline to *para*-phenylenediamine.

reaction did not proceed efficiently at room temperature, even after increasing the reaction time to 18 h (Table S3 entries 8–10, ESI†). No product formation was observed in the absence of a catalyst (Table S3 entry 3, ESI†). Next, the reaction was performed with the individual components of CCI–CN and the precursor copper salt, CuI, and none of them resulted in better yields compared to the aforementioned composite catalyst (Table S3 entries 14–16, ESI†). This obtained result can be attributed to the synergistic effects arising from the combination of the two materials, activating both the reactants simultaneously and lowering the activation energy of the reaction. The catalyst (CCI–CN) loading amount of 10 mg turned out to be the optimized one because lowering the amount resulted in a lower yield of quinazolin-4(3*H*)-ones.

The substrate scope of a variety of aldehyde derivatives was examined under the optimum conditions (Table 2). In all cases, irrespective of the nature of substituents and their positions, all tested aldehydes that react with 2-aminobenzamide afforded good-to-excellent yields in the synthesis of quinazolin-4(3*H*)-one derivatives (Table 2, entries **5aa–5aj**). The presented synthesis protocol can also tolerate heterocyclic aldehydes such as furfural (Table 2, entry **5ai**). Our catalyst system performs very efficiently to form quinazolin-4(3*H*)-one derivatives compared to most of the already reported systems (Table S5, ESI†).

Recyclability tests were conducted to investigate the sustainability of the CCI–CN catalyst. Benzonitrile and *para*-nitroaniline were taken as model substrates to study the reusability of the synthesized photocatalyst in benzonitrile hydration and *para*-nitroaniline reduction, respectively. For the synthesis of quinazolin-4(3*H*)-ones, 2-aminobenzamide and 4-methylbenzaldehyde were chosen as the model substrates to assess the recyclability efficiency (Fig. S4a, ESI†). To examine the possibility of leaching of any metal species during quinazolin-4(3*H*)-one synthesis, a hot-filtration test was performed. The reaction resulted in 40% progress within 1 h but did not proceed significantly after the removal of the catalyst, suggesting that negligible leaching of metal species occurs during the synthesis (Fig. S4b, ESI†).

3.3. Electrochemical properties

The electrochemical properties of the as-synthesized materials were evaluated using a three-electrode assembly. Cyclic voltammetry (CV) measurements were performed to investigate the charge storage behaviour of the materials. The CV curves were obtained at different scan rates (10–100 mV s^{-1}), as shown in Fig. 9(a). The quasi-rectangular shape of the CV curves suggests a combination of electric double-layer capacitance (EDLC) and pseudo-capacitance, arising from diffusion-limited processes and surface-redox properties. The specific capacitance values, calculated from the CV curves using eqn (S1) (ESI†) and plotted as a function of the scan rate, revealed that the specific capacitance decreases with increasing scan rate (Fig. 9(d)).

Table 2 Substrate scope of CCI–CN in the synthesis of quinazolin-4(3*H*)-one derivatives[a]

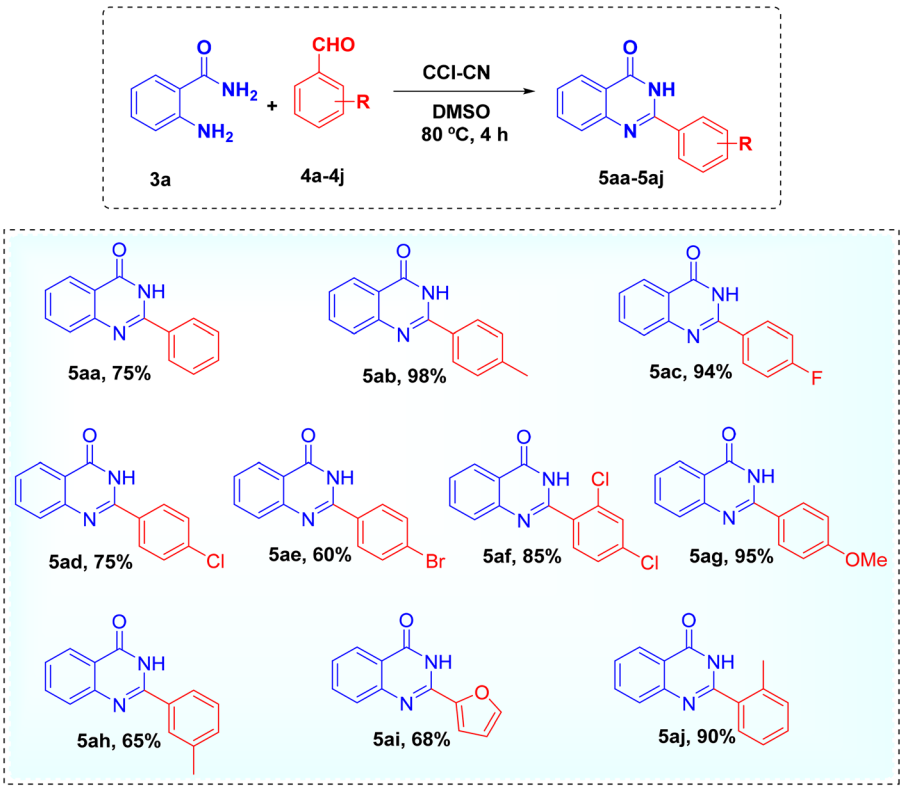

[a] Reaction conditions: 2-aminobenzamide (0.1 mmol), benzaldehyde (1.2 equivalent), and CCI–CN (10 mg) were stirred in DMSO (1 mL) for 4 h in air at 80 °C. All yields are reported as isolated yields.

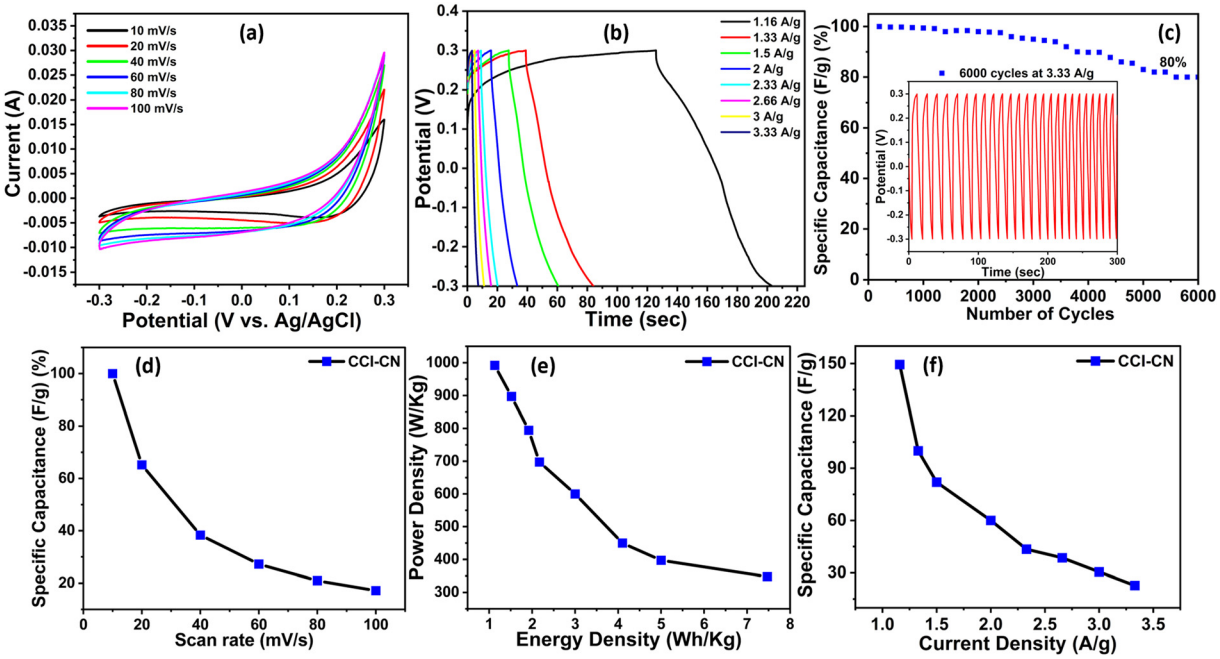

Fig. 9 (a) Cyclic voltammetry (CV) curves of CCI–CN at different scan rates. (b) Galvanostatic charge–discharge (GCD) curves of CCI–CN at different current densities. (c) Long-term cycling stability of the CCI–CN supercapacitor; inset: charge–discharge cycles after 6000 cycles showing the stability. (d) Scan rate *vs.* specific capacitance curve of the CCI–CN supercapacitor. (e) Ragone plot of the CCI–CN supercapacitor. (f) Current density *vs.* specific capacitance curve of the CCI–CN supercapacitor.

This can be attributed to the lesser time available for the effective diffusion of ion across the electrode–electrolyte interface at higher scan rates.[54]

Initially, for the quantitative examination of the charge storing capacity, the galvanostatic charge–discharge (GCD) analyses of the as-synthesized materials were carried out. The comparative GCD study of the materials reveals that the $CsCu_2I_3$@g-C_3N_4 (CCI–CN) composite shows the highest specific capacitance, outperforming $CsCu_2I_3$ and g-C_3N_4 with specific capacitances of 58.11 F g^{-1} and 19.14 F g^{-1}, respectively (Fig. 9(b) and Fig. S5, ESI†). This comparative outcome indicates the better charge storage capacity of the CCI–CN composite compared to its counterparts. Hence, we have considered the CCI–CN composite for further electrochemical studies. The specific capacitances of the as-synthesized composite were calculated from the GCD plot at different current densities using eqn (S2), ESI† (Fig. 9(b)). As shown in Fig. 9(f), the CCI–CN composite exhibits the maximum specific capacitance of 149.4 F g^{-1} at a current density of 1.16 A g^{-1}, which decreases with increasing current densities. This can be attributed to the diffusion effect, which limits the movement of electrolytic ions, thus resulting in the partial utilization of active surface sites at a high current density. Moreover, incomplete ion transport reduces the effective area for charge storage, thereby decreasing the specific capacitance.[55] The long-term stability of the composite was evaluated by performed multiple GCD cycles up to 6000 cycles, as shown in Fig. 9(c). The Ragone plot displays the correlation between the energy density and power density, as calculated using eqn (S3) and (S4), ESI† respectively (Fig. 9(e)). The as-synthesized composite delivers an exceptionally high power density value of 992 W kg^{-1}, and the corresponding energy density is 1.13 Wh kg^{-1} at a current density of 3.33 A g^{-1}. Even at a lower current density of 1.16 A g^{-1}, it manages to deliver a high power density of 347.89 W kg^{-1} and an energy density of 7.47 Wh kg^{-1}, which is better than those of other perovskites (Table S6, ESI†). This hybrid supercapacitor with a high power density is invaluable in technologies that prioritize rapid energy transfer and responsiveness over prolonged energy storage, such as vehicle regenerative braking systems, power backup systems, radar systems and lasers, and life-saving devices like defibrillators.

To further evaluate the facilitated ion-transport kinetics in the materials, Nyquist plots were obtained *via* electrochemical impedance spectroscopy (EIS), as shown in Fig. 4(d). The intercept of the Nyquist curve on the horizontal axis depicts the charge transfer resistance (CTR). The as-synthesized CCI–CN composite material shows the lowest CTR compared to its counterparts, which is very crucial for supercapacitors because fast charge transfer and low CTR enable rapid energy storage and retrieval. Efficient charge transfer leads to better utilization of the electrode material. This suggests more active sites are available for charge storage, leading to a higher specific capacitance compared to the other materials studied here.

4. Conclusions

To conclude, a lead-free Cu-based $CsCu_2I_3$@g-C_3N_4 (CCI–CN) perovskite composite was fabricated by the post-synthetic modification of lead-free perovskite $CsCu_2I_3$ (CCI) with the low-cost,

environment-friendly photocatalytic material g-C_3N_4 (CN). We investigated the unexplored research avenues, such as electrochemical and photocatalytic behaviour. Compared to many other perovskite materials, our as-synthesized CCI–CN composite exhibited an outstanding supercapacitive behaviour with a specific capacitance value of 149.4 F g^{-1} at a current density of 1.16 A g^{-1}. The composite showed an exceptionally high power density of 992 W kg^{-1} with the corresponding energy density of 1.13 Wh kg^{-1}. Further results indicated its potential to function as a hybrid supercapacitor. Besides, CCI–CN, as a heterogeneous catalyst, revealed a remarkable catalytic activity in the photo-hydration of benzonitrile and photo-reduction of *para*-nitroaniline with excellent product yields. This enhanced photocatalytic activity was attributed to the heterojunction formation at the interface, which provided a fast channel for the migration of photo-generated electrons, reducing the recombination rate compared to those of the individual components. The versatility of the CCI–CN catalyst was also tested in the synthesis of one of the most important medicinally acclaimed N-heterocyclic compounds, quinazolin-4(3*H*)-ones, with an excellent yield of up to 98%.

Author contributions

The manuscript was written with contribution from all authors. All authors have given approval to the final version of the manuscript.

Conflicts of interest

There is no conflict of interest involved in this work, and the authors declare no competing financial interests.

Data availability

The data supporting this article have been included as part of the manuscript.

Acknowledgements

M. G. is thankful to Dibrugarh University for the research fellowship. We sincerely thank DST for financial support under the DST-PURSE project (SR/PURSE/2022/143 (C)) and the DST-FIST project (SR/FST/CS-I/2020/152). We acknowledge STIC Cochin for XRD analyses, IASST Guwahati for TEM, IIT Roorkee for XPS, IIT Indore for BET analysis and the CSIC Dibrugarh University for NMR analysis.

References

1 M. Roknuzzaman, C. Zhang, K. (Ken) Ostrikov, A. Du, H. Wang, L. Wang and T. Tesfamichael, Electronic and Optical Properties of Lead-Free Hybrid Double Perovskites for Photovoltaic and Optoelectronic Applications, *Sci. Rep.*, 2019, **9**, 718.

2 X. Wang, T. Zhang, Y. Lou and Y. Zhao, All-Inorganic Lead-Free Perovskites for Optoelectronic Applications, *Mater. Chem. Front.*, 2019, **3**, 365–375.

3 G. Schileo and G. Grancini, Lead or No Lead? Availability, Toxicity, Sustainability and Environmental Impact of Lead-Free Perovskite Solar Cells, *J. Mater. Chem. C*, 2021, **9**, 67–76.

4 L. A. Muscarella and E. M. Hutter, Halide Double-Perovskite Semiconductors beyond Photovoltaics, *ACS Energy Lett.*, 2022, **7**, 2128–2135.

5 S. Ahmed, M. A. Gondal, A. S. Alzahrani, M. Parvaz, A. Ahmed and S. Hussain, Recent Trends and Challenges in Lead-Free Perovskite Solar Cells: A Critical Review, *ACS Appl. Energy Mater.*, 2024, **7**, 1382–1397.

6 G. S. H. Thien, M. Ab Rahman, B. K. Yap, N. M. L. Tan, Z. He, P.-L. Low, N. K. Devaraj, A. F. Ahmad Osman, Y.-K. Sin and K.-Y. Chan, Recent Advances in Halide Perovskite Resistive Switching Memory Devices: A Transformation from Lead-Based to Lead-Free Perovskites, *ACS Omega*, 2022, **7**, 39472–39481.

7 I. Hamdi, Y. Khan, F. Aouaini, J. H. Seo, H.-J. Koo, M. M. Turnbull, B. Walker and H. Naïli, A Copper-Based 2D Hybrid Perovskite Solar Absorber as a Potential Eco-Friendly Alternative to Lead Halide Perovskites, *J. Mater. Chem. C*, 2022, **10**, 3738–3745.

8 H. Lee, D. Lee, H. Jin, D. Baek, M. K. Kim, J. Cha, S.-K. Kim and M. Kim, Optical Humidity Sensors Based on Lead-Free Cu-Based Perovskite Nanomaterials, *Nanoscale Adv.*, 2022, **4**, 3309–3317.

9 Y. Zhang, J. Guo, Y. Liu, J. Wang, P. Wang, H. Chen, H. Li and S. Chen, Unveiling the Underlying Mechanism behind the Greatly Increased Properties of Cu(I)–Perovskites and Their Applications for Durable WLED and Multi-Model Encryption/Decryption, *Chem. Eng. J.*, 2023, **472**, 144812.

10 J. Li, J. Duan, X. Yang, Y. Duan, P. Yang and Q. Tang, Review on Recent Progress of Lead-Free Halide Perovskites in Optoelectronic Applications, *Nano Energy*, 2021, **80**, 105526.

11 T. Miyasaka, A. Kulkarni, G. M. Kim, S. Öz and A. K. Jena, Perovskite Solar Cells: Can We Go Organic-Free, Lead-Free, and Dopant-Free?, *Adv. Energy Mater.*, 2020, **10**, 1902500.

12 J. Wen, K. Rong, L. Jiang, C. Wen, B. Wu, B. Sa, Y. Qiu and R. Ahuja, Copper-Based Perovskites and Perovskite-like Halides: A Review from the Perspective of Molecular Level, *Nano Energy*, 2024, **128**, 109802.

13 J.-W. Shi, Y. Zou, L. Cheng, D. Ma, D. Sun, S. Mao, L. Sun, C. He and Z. Wang, In-Situ Phosphating to Synthesize Ni_2P Decorated NiO/g-C_3N_4 p–n Junction for Enhanced Photocatalytic Hydrogen Production, *Chem. Eng. J.*, 2019, **378**, 122161.

14 Z. Pu, B. Xiao, S. Mao, Y. Sun, D. Ma, H. Wang, J. Zhou, Y. Cheng and J.-W. Shi, An Electron-Hole Separation Mechanism Caused by the Pseudo-Gap Formed at the Interfacial Co–N Bond between Cobalt Porphyrin Metal Organic Framework and Boron-Doped g-C_3N_4 for Boosting Photocatalytic H_2 Production, *J. Colloid Interface Sci.*, 2022, **628**, 477–487.

15 L. Romani, A. Speltini, C. N. Dibenedetto, A. Listorti, F. Ambrosio, E. Mosconi, A. Simbula, M. Saba, A. Profumo,

P. Quadrelli, F. De Angelis and L. Malavasi, Experimental Strategy and Mechanistic View to Boost the Photocatalytic Activity of $Cs_3Bi_2Br_9$ Lead-Free Perovskite Derivative by g-C_3N_4 Composite Engineering, *Adv. Funct. Mater.*, 2021, **31**, 2104428.

16 M. Zhang, Y. Yang, X. An, J. Zhao, Y. Bao and L. Hou, Exfoliation Method Matters: The Microstructure-Dependent Photoactivity of g-C_3N_4 Nanosheets for Water Purification, *J. Hazard. Mater.*, 2022, **424**, 127424.

17 F. Dong, Y. Li, Z. Wang and W.-K. Ho, Enhanced Visible Light Photocatalytic Activity and Oxidation Ability of Porous Graphene-like g-C_3N_4 Nanosheets *via* Thermal Exfoliation, *Appl. Surf. Sci.*, 2015, **358**, 393–403.

18 K. Song, J. Gou, L. Yang and C. Zeng, Environmentally Stable Mesoporous g-C_3N_4 Modified Lead-Free Double Perovskite $Cs_2AgBiBr_6$ for Highly Efficient Photocatalytic Hydrogen Evolution, *Catal. Lett.*, 2023, **153**, 534–543.

19 Z.-J. Bai, Y. Mao, B.-H. Wang, L. Chen, S. Tian, B. Hu, Y.-J. Li, C.-T. Au and S.-F. Yin, Tuning Photocatalytic Performance of $Cs_3Bi_2Br_9$ Perovskite by g-C_3N_4 for $C(Sp^3)$–H Bond Activation, *Nano Res.*, 2023, **16**, 6104–6112.

20 F. Yu, Z. Wang, S. Zhang, H. Ye, K. Kong, X. Gong, J. Hua and H. Tian, Molecular Engineering of Donor–Acceptor Conjugated Polymer/g-C_3N_4 Heterostructures for Significantly Enhanced Hydrogen Evolution Under Visible-Light Irradiation, *Adv. Funct. Mater.*, 2018, **28**, 1804512.

21 B. Wang, D. Chen, N. Li, Q. Xu, H. Li, J. He and J. Lu, Enhanced Photocatalytic Oxidation of Nitric Oxide to MOF-Derived Hollow Bimetallic Oxide Microcubes Supported on g-C_3N_4 Nanosheets *via* p–n Heterojunction, *Ind. Eng. Chem. Res.*, 2021, **60**, 2921–2930.

22 M. Prejanò, M. E. Alberto, N. Russo and T. Marino, Hydration of Aromatic Nitriles Catalyzed by Mn-OH Complexes: A Rationalization from Quantum Chemical Investigations, *Organometallics*, 2020, **39**, 3352–3361.

23 M. Trivedi, S. K. Dubey, G. Kaur and N. P. Rath, Ru(II)- and Ru(IV)-dmso Complexes Catalyze Efficient and Selective Aqueous-Phase Nitrile Hydration Reactions under Mild Conditions, *New J. Chem.*, 2021, **45**, 17339–17346.

24 R. Pollet, M. Andronaco and H. S. Biswal, Onset of Nitriles Hydration with an Environmentally Benign Catalyst: In-Water *versus* on-Water Conditions, *ChemPhysChem*, 2024, **25**, 202400108.

25 W. Oberhauser, M. Bartoli, G. Petrucci, D. Bandelli, M. Frediani, L. Capozzoli, C. Cepek, S. Bhardwaj and L. Rosi, Nitrile Hydration to Amide in Water: Palladium-Based Nanoparticles *vs.* Molecular Catalyst, *J. Mol. Catal. A: Chem.*, 2015, **410**, 26–33.

26 Y. Bi, Z. Huang, T. Bian, Q. Zhang, Y. Yu, T. Zhang, Z. Lin, T. Chen, Z. Chen, Y. Bu and J. Jiang, Explosibility and Thermal Decomposition Behavior of Nitrile Rubber Dust in Industrial Processes, *J. Loss Prev. Process. Ind.*, 2023, **84**, 105136.

27 K. Revathi, S. Palantavida and B. Kizhakkekilikoodayil Vijayan, Effective Reduction of P-Nitroaniline to p-Phenylenediamine Using Cu–CuO Nanocomposite, *Mater. Today:. Proc.*, 2019, **9**, 633–638.

28 J. Wei, Y. Chen, H. Zhang, Z. Zhuang and Y. Yu, Hierarchically Porous S-Scheme CdS/UiO-66 Photocatalyst for Efficient 4-Nitroaniline Reduction, *Chin. J. Catal.*, 2021, **42**, 78–86.

29 M. A. Ojong, N. Mujafarkani, F. A. K. Khazaal, A. S. Hussam, O. C. Godfrey, K. Muzammil, A. J. Ahamed, R. U. Edadi, I. A. Anyambula, E. Moses and I. Benjamin, Investigating the Impact of Solvation on *P*-Phenylenediamine-2-Amino Pyrimidine-Formaldehyde Terpolymer (P2APF) Ligand's Reactivity and Drug Suitability for Malaria Treatment: Insights from Experimental and Quantum Calculations, *J. Mol. Struct.*, 2024, **1310**, 138113.

30 A. Meyer and K. Fischer, Oxidative Transformation Processes and Products of Para-Phenylenediamine (PPD) and Para-Toluenediamine (PTD)-a Review, *Environ. Sci. Eur.*, 2015, **27**, 11.

31 D. Sarma, B. Majumdar, B. Deori, S. Jain and T. K. Sarma, Photoinduced Enhanced Decomposition of TBHP: A Convenient and Greener Pathway for Aqueous Domino Synthesis of Quinazolinones and Quinoxalines, *ACS Omega*, 2021, **6**, 11902–11910.

32 Z. Xie, J. Lan, H. Zhu, G. Lei, G. Jiang and Z. Le, Visible Light Induced Tandem Reactions: An Efficient One Pot Strategy for Constructing Quinazolinones Using in-Situ Formed Aldehydes under Photocatalyst-Free and Room-Temperature Conditions, *Chin. Chem. Lett.*, 2021, **32**, 1427–1431.

33 Z. Xie, J. Lan, L. Yan, X. Chen, Q. Li, J. Meng and Z. Le, Photocatalyst-Free Visible-Light-Promoted Quinazolinone Synthesis at Room Temperature Utilizing Aldehydes Generated *in Situ via* C=C Bond Cleavage, *Org. Biomol. Chem.*, 2021, **19**, 2436–2441.

34 A. M. Alsibaee, H. M. Al-Yousef and H. S. Al-Salem, Quinazolinones, the Winning Horse in Drug Discovery, *Molecules*, 2023, **28**, 978.

35 S. K. Wahan, B. Sharma and P. A. Chawla, Medicinal Perspective of Quinazolinone Derivatives: Recent Developments and Structure–Activity Relationship Studies, *J. Heterocycl. Chem.*, 2022, **59**, 239–257.

36 A. Yadav, F. N. Mansoorie, A. Saini and M. Bag, Vacancy Ordered Lead Free Double Perovskite Based Flexible Supercapacitor for Sustainable Energy Applications, *ACS Sustainable Chem. Eng.*, 2024, **12**, 1029–1037.

37 S. H. S. Pai, A. Sasmal, A. K. Nayak and H. Han, Facile Solvothermal Synthesis of NiO/g-C_3N_4 Nanocomposite for Enhanced Supercapacitor Application, *Int. J. Energy Res.*, 2023, **2023**, 1524859.

38 A. Yadav, A. Saini, P. Kumar and M. Bag, Lead-Free Halide Perovskites for High-Performance Thin-Film Flexible Supercapacitor Applications, *J. Mater. Chem. C*, 2024, **12**, 197–206.

39 S. Güz, M. Buldu-Akturk, H. Göçmez and E. Erdem, All-in-One Electric Double Layer Supercapacitors Based on $CH_3NH_3PbI_3$ Perovskite Electrodes, *ACS Omega*, 2022, **7**, 47306–47316.

40 C. Wang, Y. Ding, Z. Xie, Y. Wang, Y. Li, N. Han, Q. Xu, Y. Lai, M. K. H. Leung, B. Liu, B.-L. Su and Y. H. Ng, Surface and Defect Engineering Coupling of Charge Shuttle and

Redox Site in $Cs_3Bi_2Br_9$/g-C_3N_4 for Efficient Photocatalytic C(sp^3)–H Bond Activation, *ACS Mater. Lett.*, 2025, **7**, 610–619.

41 J. Zhou, B. Gao, D. Wu, C. Tian, H. Ran, W. Chen, Q. Huang, W. Zhang, F. Qi, N. Zhang, Y. Pu, J. Qiu, Z. Hu, J. Du, Z. Liu, Y. Leng and X. Tang, Enhanced Photocatalytic Activity of Lead-Free Cs_2TeBr_6/g-C_3N_4 Heterojunction Photocatalyst and Its Mechanism, *Adv. Funct. Mater.*, 2024, **34**, 2308411.

42 Y. Lv, D. Ma, C. Yang, K. Song, L. Shi, Y. Cheng, C. Niu and J.-W. Shi, In-situ construction of lead-free halide perovskite $CsCu_2I_3$/g-C_3N_4 heterojunction for photocatalytic H_2 generation, *Sep. Purif. Technol.*, 2023, **316**, 123813.

43 A. Dutta, S. Mitra, M. Basak and T. Banerjee, A Comprehensive Review on Batteries and Supercapacitors: Development and Challenges since Their Inception, *Energy Storage*, 2023, **5**, 339.

44 L. Li, Z. Fan, J. Zhang, D. Fan, X. Liu and Y. Wang, Yellow Emissive $CsCu_2I_3$ Nanocrystals Induced by Mn^{2+} for High-Resolution X-Ray Imaging, *Inorg. Chem.*, 2023, **62**, 19848–19855.

45 D. N. Sutar, A. K. Pramod, H. Islam, A. V. Sesha Sainath, U. Pal and S. K. Batabyal, $Cs_3Bi_2Cl_3Br_6$:g-C_3N_4 Nanostructure-Based Thin Film Photocatalysts for Hydrogen Production under Daylight and Simulated Light, *ACS Appl. Nano Mater.*, 2024, **7**, 25556–25568.

46 C. F. Holder and R. E. Schaak, Tutorial on Powder X-Ray Diffraction for Characterizing Nanoscale Materials, *ACS Nano*, 2019, **13**, 7359–7365.

47 I. A. Mudunkotuwa, A. A. Minshid and V. H. Grassian, ATR-FTIR Spectroscopy as a Tool to Probe Surface Adsorption on Nanoparticles at the Liquid–Solid Interface in Environmentally and Biologically Relevant Media, *Analyst*, 2014, **139**, 870–881.

48 M. Roškarič, J. Zavašnik, D. Zámbó, T. Kotnik, S. Kovačič, G. Žerjav and A. Pintar, Optimization Method Based on Simplex for Surface Area Improved Photocatalytic Performance of g-C_3N_4, *ACS Catal.*, 2023, **13**, 13282–13300.

49 I. Grigioni, M. Abdellah, A. Corti, M. V. Dozzi, L. Hammarström and E. Selli, Photoinduced Charge-Transfer Dynamics in WO_3/$BiVO_4$ Photoanodes Probed through Midinfrared Transient Absorption Spectroscopy, *J. Am. Chem. Soc.*, 2018, **140**, 14042–14045.

50 P. Vashishtha, G. V. Nutan, B. E. Griffith, Y. Fang, D. Giovanni, M. Jagadeeswararao, T. C. Sum, N. Mathews, S. G. Mhaisalkar, J. V. Hanna and T. White, Cesium Copper Iodide Tailored Nanoplates and Nanorods for Blue, Yellow, and White Emission, *Chem. Mater.*, 2019, **31**, 9003–9011.

51 W. Fan, L. Xu, Z. Yang, Y. Liu and J. Song, A-Site FA^+ Engineering Boosting Photoluminescence Efficiency and Stability of Cesium Copper Iodine ($Cs_3Cu_2I_5$) Perovskites, *J. Mater. Chem. C*, 2023, **11**, 1076–1081.

52 G. Deroubaix and P. Marcus, X-Ray Photoelectron Spectroscopy Analysis of Copper and Zinc Oxides and Sulphides, *Surf. Interface Anal.*, 1992, **18**, 39–46.

53 X. Sun, J. Yang, Z. Wu, G. Meng, X. Guo, D. Kuang, L. Xiong, W. Qu, X. Fang, X. Yang, X. Tang and Y. He, Lead-Free $CsCu_2I_3$ Perovskite Nanostructured Networks Gas Sensor for Selective Detection of Trace Nitrogen Dioxide at Room Temperature, *IEEE Sens. J.*, 2021, **21**, 14677–14684.

54 R. Kumar and M. Bag, Quantifying Capacitive and Diffusion-Controlled Charge Storage from 3D Bulk to 2D Layered Halide Perovskite-Based Porous Electrodes for Efficient Supercapacitor Applications, *J. Phys. Chem. C*, 2021, **125**, 16946–16954.

55 S. Verma, A. Singh, S. Khajuria, A. Sharma, P. Mahajan, B. Singh and S. Arya, Sol–Gel Synthesized Carbon Nanoparticles as Supercapacitor Electrodes with Ultralong Cycling Stability, *Fullerenes, Nanotubes, Carbon Nanostruct.*, 2021, **29**, 1045–1052.

